

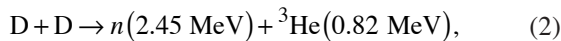
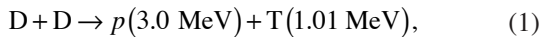
---

# Proton Temporal Diagnostic for ICF Experiments on OMEGA

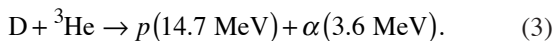
## Introduction

In an inertial confinement fusion (ICF)<sup>1</sup> experiment, a capsule filled with deuterium (D<sub>2</sub>) or a deuterium–tritium (DT) fuel is heated by either direct laser illumination or soft-x-ray radiation in a laser-heated hohlraum. The target is compressed to conditions under which thermonuclear fusion occurs. The fusion burn begins with spark ignition of the central hot spot<sup>2</sup> that is created by shock convergence (shock burn). A burn wave then propagates into the compressed dense fuel regions, releasing energy through fusion reactions (compressive burn).<sup>2</sup> Both a high-temperature hot spot and high areal density are necessary in cryogenic DT implosions to ignite the target and achieve high gain.<sup>1–3</sup>

Experimental information about implosion dynamics is crucial for understanding capsule fuel assembly and validating numerical simulations. Areal-density evolution measurements in cryogenic D<sub>2</sub> or DT implosions are complicated by the lack of simple and reliable diagnostic techniques that are available with plastic-shell targets. Therefore, many experimental studies in ICF are performed with hydrodynamically equivalent “cryogenic surrogates” such as thick plastic shells filled with D<sup>3</sup>He or D<sub>2</sub> fuel. The primary fusion reactions that occur in imploding capsules fueled with D<sup>3</sup>He gas are



and

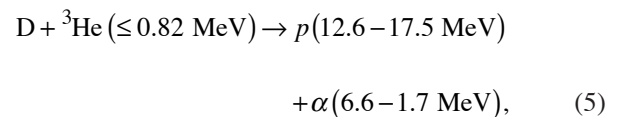
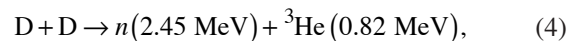


From reactions (1)–(3) one can see that with D<sup>3</sup>He both neutron diagnostics and charged-particle spectroscopy<sup>4</sup> can be used on OMEGA<sup>5</sup> to probe the plasma conditions during the shock and compressive burn phases of an implosion.

The capsule burn history is an important measure of target performance and implosion dynamics and is directly compa-

table with numerical models. The neutron burn history is measured on OMEGA (and previously on the Nova laser at LLNL) using the streak camera–based neutron temporal diagnostic (NTD)<sup>6,7</sup> with a time resolution of ~50 ps for DD neutrons and ~25 ps for DT neutrons. The neutron burn history contains valuable information about the capsule implosion close to the peak of compression. Since the neutron yield at shock convergence is about 100 times smaller than the yield at peak compression, it is difficult to measure the neutron shock signal using the NTD. On the other hand, the primary proton shock and compression yields are comparable in a typical D<sup>3</sup>He implosion on OMEGA.<sup>8</sup> To use this unique feature of the D<sup>3</sup>He fuel, a proton temporal diagnostic (PTD), based on the NTD concept, has been developed for implosion studies at OMEGA. The PTD allows us to record the proton-production history and simultaneously measure shock bang time and compression bang time in a D<sup>3</sup>He implosion. Protons emitted from the D<sup>3</sup>He reaction lose energy when passing through the compressed capsule shell. The areal density of target material through which the protons pass determines the amount of energy loss. Therefore, by measuring the proton-production history with the PTD and simultaneously a time-integrated proton-energy spectrum by charged-particle spectroscopy, the temporal evolution of target areal density is inferred. The areal-density evolution in D<sup>3</sup>He implosions was first studied in Ref. 9 with the assumption that the D<sup>3</sup>He–proton-production history is proportional to the D<sub>2</sub>–neutron-production history. With the development of the PTD, areal-density evolution can now be inferred using the proton-production history.<sup>10</sup>

The PTD was developed primarily for D<sup>3</sup>He implosions; however, the PTD is also sensitive to secondary protons and primary neutrons from D<sub>2</sub>-fueled implosions. The PTD reactions of interest in a D<sub>2</sub> implosion are the following:



where reaction (4) is the primary reaction and (5) is the secondary. An average areal density can be inferred from the time difference of the secondary proton and primary neutron signals in the PTD.

**The PTD Detector System**

The PTD detector system was developed as a modification of the existing OMEGA neutron temporal diagnostic—the cryoNTD.<sup>7</sup> This diagnostic was designed to operate in one of the OMEGA ten-inch manipulators (TIM’s). The PTD system, shown schematically in Fig. 96.24, is based on a fast scintillator (BC-422) that acts as a proton-to-light converter shielded by a thin (100- to 200- $\mu\text{m}$ ) foil against x-ray and direct laser illumination. The optical system, consisting of 11 lenses and 2 mirrors, is described in detail in Ref. 7. It transfers the scintillator light through the TIM and the vacuum window along a 3.5-m optical path to a high-speed optical streak camera<sup>11</sup> for recording. The front end of the optical system is mounted in the TIM and inserted close to the target. Since the PTD uses the existing cryoNTD optics and mechanical assembly, the current PTD scintillator is located 9 cm from the target, which is the required standoff distance for OMEGA cryogenic target operations. With additional optics, the PTD scintillator can be placed closer to noncryogenic targets. A simultaneously recorded optical fiducial provides a reference for accurate timing with respect to the incident laser pulse. Figure 96.25 shows a sample image recorded by a charge-coupled-device (CCD) camera attached to the streak camera for a D<sup>3</sup>He

implosion with a proton yield of  $5.7 \times 10^7$ . The horizontal axis in the image corresponds to time. The fiducial train is seen on top of the image and the scintillator output in the center. The PTD signal is averaged across the central portion of the scintillator, and the CCD background from the bottom portion of the image is subtracted to create the final temporal trace. The streak camera flat-field and geometric distortions are included in the signal processing.

**The PTD Nose Cone**

The nose cone is the main difference between the PTD and the cryoNTD.<sup>7</sup> The design of the PTD nose cone must satisfy several criteria: it must (1) be light tight to prevent direct laser illumination; (2) be able to sustain ablation, target debris, and the thermal impulse from the target implosion; (3) be transparent to protons with energies larger than 10 MeV; and (4) absorb as much of the soft-x-ray radiation as possible. The last requirement leads to a filter made from a high-Z material. Tantalum was chosen as the PTD filter material because of its strength and hardness and because 25-mm-diam tantalum foil disks are available commercially.<sup>12</sup> To avoid scintillator melting, a 0.3-mm-thick ultem plastic spacer ring was inserted between the filter foil and the scintillator. Without the spacer ring, the BC-422 scintillator is subject to a thermal impulse and may melt as a consequence. The final design of the PTD nose cone is shown in Fig. 96.26. The threaded retainer ring accommodates filter foils and scintillators of different thicknesses. The PTD nose cone itself is attached to the front end of the PTD

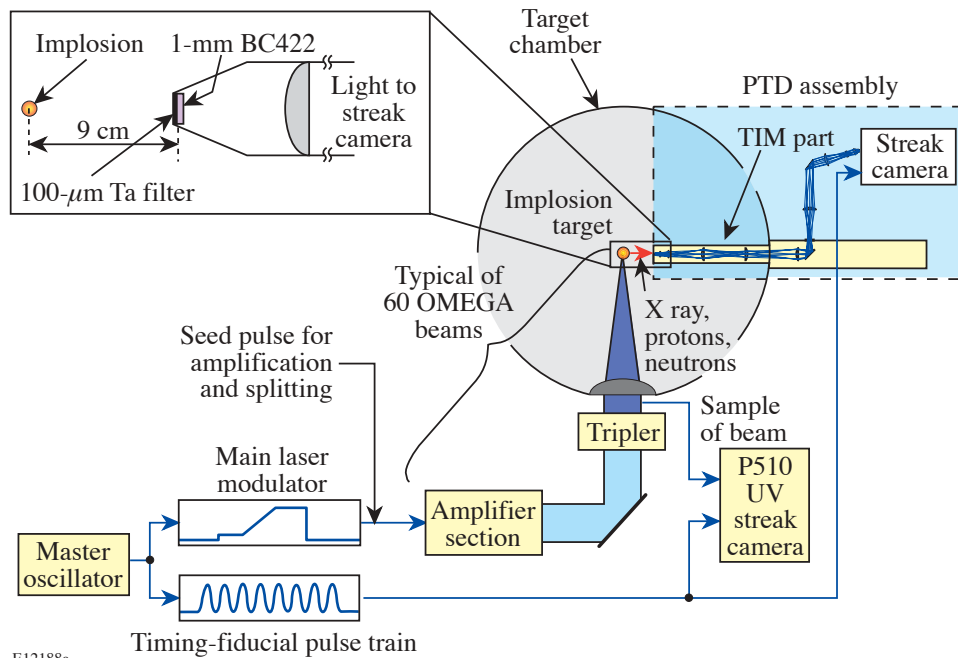


Figure 96.24 Block diagram of the PTD detector system integrated into the OMEGA facility. The fiducial system provides cross-timing between the neutron and proton signals and the incident laser pulse, which is recorded on the P510 UV streak camera.

E12188a

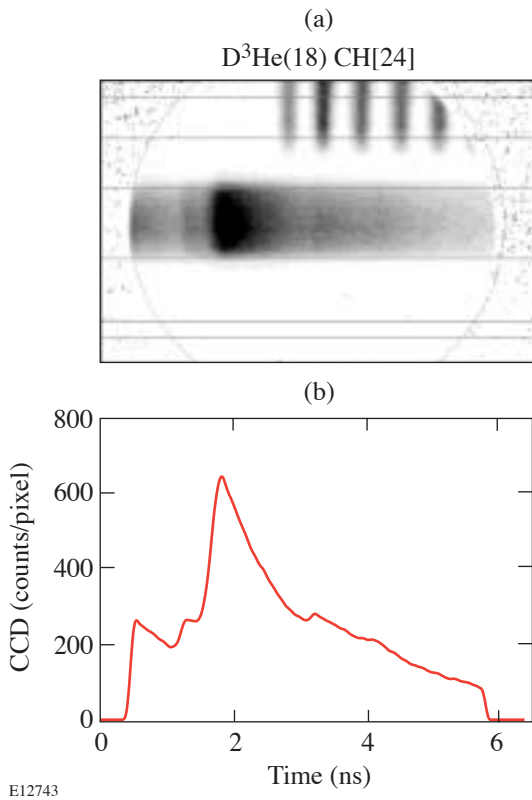


Figure 96.25  
 (a) The PTD streak camera image from shot #29962 in which a 24- $\mu\text{m}$ -thick plastic shell filled with 18 atm of  $\text{D}^3\text{He}$  was imploded on OMEGA with a 1-ns pulse shape and 23 kJ of energy; (b) the PTD signal averaged across the central portion of the scintillator with the CCD background subtracted and the streak camera flat-field and geometric distortions taken into account.

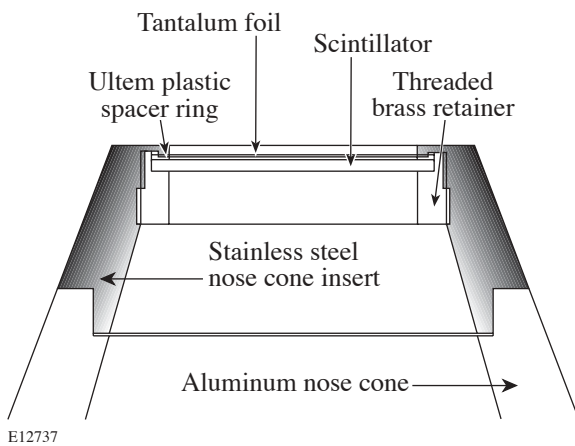


Figure 96.26  
 A cross-section schematic of the PTD nose cone.

mechanical assembly by two latches. It is possible to change the PTD nose cone to the cryoNTD nose cone or to change the PTD filter foil/scintillator within the 45-min OMEGA shot cycle. Tests done with 100- $\mu\text{m}$  Ta foils placed 9 cm from the target show that these foils can survive more than 50 direct-drive OMEGA shots without damage.

**The PTD Background**

Several sources of background affect the PTD measurements. The soft and hard x rays from a target implosion reach the PTD scintillator at 9 cm from the target about 1.4 ns before the  $\text{D}^3\text{He}$  protons. The BC-422 scintillator has a very fast rise time (<20 ps) and a decay time of  $\sim 1.2$  ns. The scintillator decay from x rays creates a background for the proton signal. Suprathermal electrons from the two-plasmon-decay (TPD) instability are another source of background in the PTD.<sup>13</sup> These electrons create hard x rays by bremsstrahlung interactions in the target and in the PTD filter foil. Since it is difficult to calculate the PTD background level, the filter thickness was optimized experimentally. The PTD background depends on many parameters such as the laser energy, pulse shape, and target design. The filter-thickness optimization required a series of identical shots where all parameters except the filter thickness were fixed. Figure 96.27 shows the PTD signal for

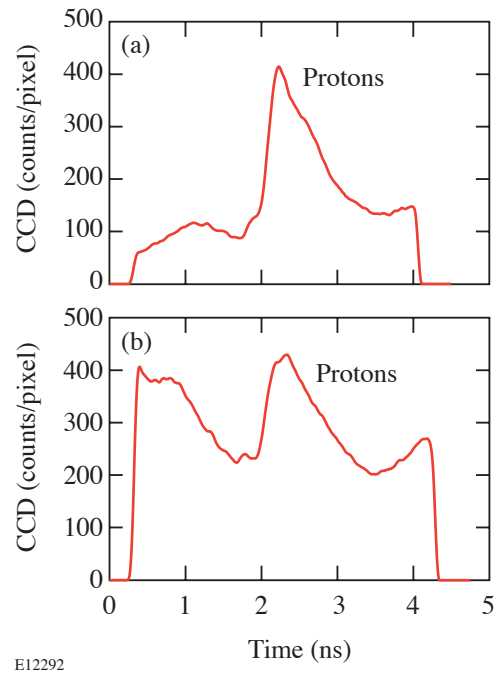


Figure 96.27  
 The PTD signals from two identical  $\text{D}^3\text{He}$  implosions. Minimum x-ray background is observed with the 100- $\mu\text{m}$  Ta filter in (a), while the background increases significantly with the thinner 50- $\mu\text{m}$  Ta filter in (b).

two identical  $D^3He$  implosions and tantalum-filter thicknesses of 100 and 50  $\mu m$ . The PTD background level with the 50- $\mu m$  Ta filter is about four times higher than with the 100- $\mu m$  Ta filter. This means that a Ta thickness of 50  $\mu m$  is not adequate to absorb the soft x rays from target implosions. Figure 96.28 shows the PTD signal for two identical  $D_2$  implosions and 100- and 200- $\mu m$  tantalum-filter thicknesses. As expected, the area under the neutron peak remained unchanged, the area under the secondary proton peak decreased (indicating that the thicker filter was stopping some fraction of the proton spectrum), and the background level decreased only marginally. A 100- $\mu m$ -thick filter appears to absorb the bulk of the soft-x-ray contribution, while the hard-x-ray contribution from TPD is only minimally affected by the thicker filter; therefore, the 100- $\mu m$  tantalum filter is close to the optimal for PTD operation.

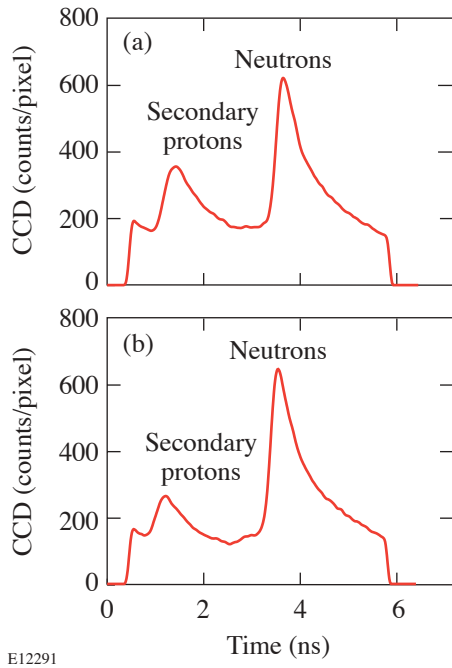


Figure 96.28  
The PTD signals from two identical  $D_2$  implosions. The background level decreases only marginally with filter-thickness increase from 100  $\mu m$  Ta in (a) to 200  $\mu m$  Ta in (b), while the secondary-proton signal decreases substantially.

The filter-thickness optimization discussed above was based on OMEGA operations prior to June 2003, when new distributed phase plates (DPP's) were installed and the standard spherical target diameter was reduced from 940 to 880  $\mu m$ . As a result of this change, the total overlapping-beam intensity on a spherical target increased from  $8.0 \times 10^{14} \text{ W/cm}^2$  to  $9.4 \times 10^{14} \text{ W/cm}^2$ , and, as was shown in Ref. 13, suprathermal

electrons generated from TPD increased by approximately a factor of 4. Following this change, the PTD background level increased by factor of 4, as can be seen in Fig. 96.29, where the PTD signal is shown for two OMEGA implosions using 19- $\mu m$ -thick CH shells and 15-atm- $D_2$  fills: (a) one before the new DPP's were installed and (b) one after installation. Tests showed that suprathermal electrons hitting the Ta filter were the main contributor to the background increase. To decrease the background level, an additional 100- $\mu m$  aluminum filter was added in front of the 100- $\mu m$  Ta filter. The low- $Z$  aluminum filter absorbs suprathermal electrons before they produce hard x rays in the Ta foil. The additional aluminum filter decreased the background level by about a factor of 4, as shown in Fig. 96.30 where the PTD signal is shown for two OMEGA implosions using 27- $\mu m$ -thick CH shells and 15-atm- $D_2$  fills: one with 100  $\mu m$  of Ta and one with a sandwich of 100  $\mu m$  of Al and 100  $\mu m$  of Ta. The additional aluminum filter also decreases the proton signal by 10% to 20% depending on the proton energy. A 100- $\mu m$  beryllium filter was also tested and found to be less effective at background reduction than the aluminum. The current PTD filter used on OMEGA consists of a sandwich of 100  $\mu m$  of Al and 100  $\mu m$  of Ta.

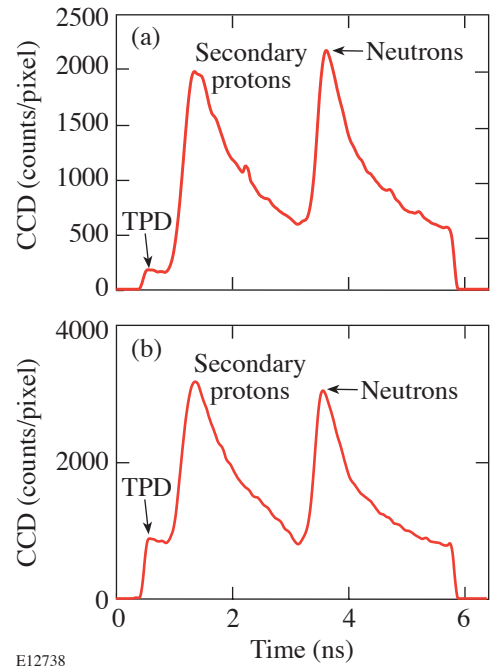
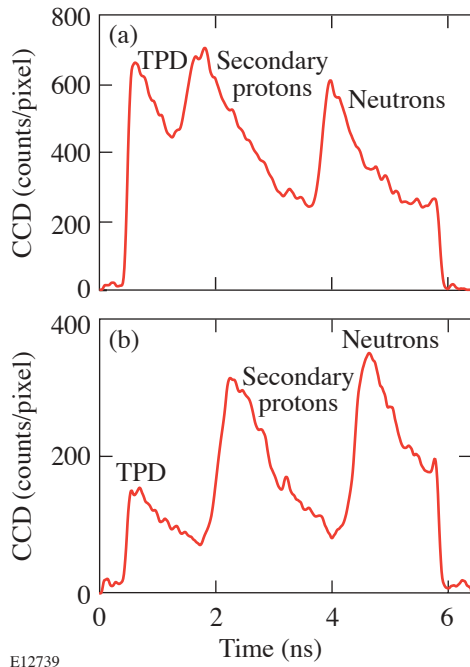


Figure 96.29  
The PTD signals from two implosions of 19- $\mu m$ -thick plastic shells filled with 15 atm of  $D_2$ . The PTD background level is four times smaller in (a), where the overlapping beam intensity is  $8.0 \times 10^{14} \text{ W/cm}^2$  in comparison with (b), where the overlapping beam intensity is  $9.4 \times 10^{14} \text{ W/cm}^2$ .



E12739

Figure 96.30

The PTD signals from two implosions of 27- $\mu\text{m}$ -thick plastic shells filled with 15 atm of  $\text{D}_2$ . Overlapping beam intensity is  $9.4 \times 10^{14} \text{ W/cm}^2$ . The PTD background level is four times higher with the 100- $\mu\text{m}$  Ta filter in (a) than with a filter consisting of a 100- $\mu\text{m}$  Al foil + 100- $\mu\text{m}$  Ta foil in (b).

### Data Analysis and Calibration

The time history of the scintillator signal is the convolution of the proton temporal distribution with the scintillator response. The actual proton burn history in the PTD is obtained by deconvolving the effect of the long scintillator decay from the recorded signal as described in Ref. 7.

Absolute timing is established using the OMEGA fiducial system. The OMEGA fiducial consists of a series of eight pulses spaced 548 ps apart and is synchronized to the shaped OMEGA laser pulse with a jitter of less than 20 ps. The optical fiducial is amplified separately from the main laser pulse, split, and distributed to various diagnostic instruments for precision timing. The fiducial pulse train is also recorded on the P510 ultraviolet streak cameras,<sup>14</sup> which record the laser pulse shapes of each beam. The common optical fiducial serves as a reference for both the proton signal and the laser pulse, thus enabling very accurate timing of the PTD signals relative to the laser pulse. The recorded fiducial pulse is fitted by a pulse train of eight Gaussian pulses spaced at a well-characterized period of 548 ps. This reduces the influence of noise on the determination of the timing reference.

Since the cryoNTD<sup>7</sup> was designed to measure only  $\text{D}_2$  neutrons from cryogenic implosions at a fixed standoff distance, the fiducial requires only a single fiber delay to align the pulse train with the neutron signal. The PTD, on the other hand, is designed for multiple fusion reaction products and multiple standoff distances. Therefore, the PTD fiducial has ten delay fibers with nominal delays from 1 ns to 10 ns with a step of 1 ns. The delay fibers were characterized at LLNL with an accuracy less than 3 ps. Using the delay fibers, the PTD fiducial train position can be adjusted for x rays,  $\text{D}^3\text{He}$  protons, DD and DT neutrons, and a change of the PTD standoff distance.

The PTD streak camera has 3 $\times$ , 5 $\times$ , and 10 $\times$  sweep cards that create approximately 3-ns, 5-ns, and 10-ns time windows with pixel resolutions of 7.5 ps, 13 ps, and 23 ps, respectively. The streak camera was carefully flat fielded with OMEGA fiducial pulses for each sweep card using the procedure described in Ref. 14. The streak camera flat-field and geometric distortions are included in the signal processing.

The PTD timing calibration was performed with a 100- $\mu\text{m}$  aluminum filter using a 100-ps laser pulse on a spherical gold target to generate a short, intense x-ray pulse. The typical PTD calibration signal at 9 cm from the target is shown in Fig. 96.31(a), and the NTD<sup>6</sup> calibration signal with a similar aluminum nose cone at 2 cm from the target is shown in Fig. 96.31(b). Comparison of the PTD and the NTD signals confirms the presence of hot electrons with energies of 100 to 300 keV in the calibration shots. The time-of-flight difference between x rays and hot electrons with 100-keV energy is 55 ps for the NTD standoff distance of 2 cm and 245 ps for the PTD standoff distance of 9 cm. This time-of-flight difference explains the falling-edge pulse shape differences between the NTD and the PTD in the calibration shots. In three shots, the PTD was calibrated relative to the OMEGA laser with an rms accuracy of  $\sim 5$  ps.

### The PTD in $\text{D}^3\text{He}$ Implosions

The main purpose of the PTD is to measure shock-time and areal-density evolution in  $\text{D}^3\text{He}$  implosions. A series of direct-drive implosions were conducted on OMEGA with 60 beams of frequency-tripled (351-nm) UV light in a 1-ns square pulse and a total energy of 23 kJ. Full smoothing of the laser beams was used,<sup>15</sup> and beam-to-beam energy imbalance was typically  $< 5\%$  rms. Three types of capsule designs were used, all with nominal diameters of 940  $\mu\text{m}$  and plastic (CH)-shell thicknesses of 20  $\mu\text{m}$ , 24  $\mu\text{m}$ , and 27  $\mu\text{m}$ . All of the capsules were filled with 6 atm of  $\text{D}_2$  and 12 atm of  $^3\text{He}$ . A typical PTD image of one of the imploded capsules with a 24- $\mu\text{m}$ -thick

plastic shell is shown in Fig. 96.25. The deconvolved proton burn history for this shot is compared in Fig. 96.32 with the burn histories from implosions using 20- $\mu\text{m}$ - and 27- $\mu\text{m}$ -thick shells. With a 5-ns time window, the PTD pixel time resolution of 13 ps is sufficient to resolve the shock coalescence and compression peaks in these  $\text{D}^3\text{He}$  implosions. It is evident

from Fig. 96.32 that the ratio of the shock yield to the compression yield in a  $\text{D}^3\text{He}$  implosion is a function of shell thickness and increases with shell thickness. A comparison of the PTD data with wedged-range-filter (WRF) spectrometer data<sup>4,8</sup> shows that the shock peak is much more evident in the PTD data than in the WRF spectrometers.

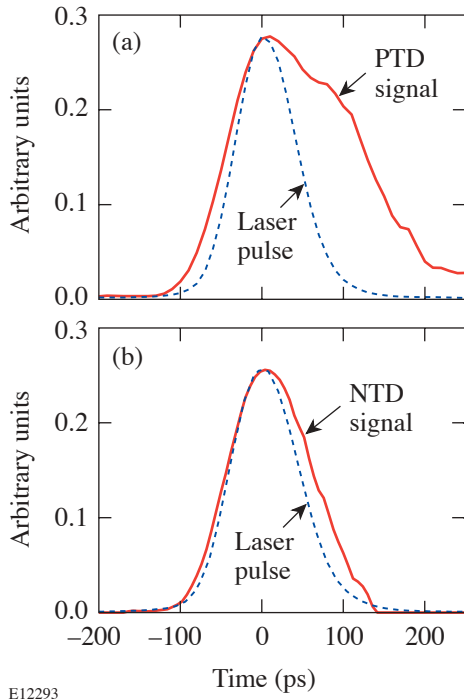


Figure 96.31  
The PTD and NTD calibration signals with a 100-ps laser pulse (dashed line): (a) PTD signal (solid line) at 9 cm from a target; (b) NTD signal (solid line) at 2 cm from a target.

The primary  $\text{D}^3\text{He}$  proton yield is inferred by integrating the area under the proton shock and compression peaks. The number of CCD counts in the PTD for the 1-mm BC-422 scintillator and the filter configuration of 100  $\mu\text{m}$  of Al + 100  $\mu\text{m}$  of Ta is plotted against the absolute yield from the WRF spectrometers in Fig. 96.33. The PTD can measure primary  $\text{D}^3\text{He}$  proton yields and proton bang time above  $1 \times 10^7$ .

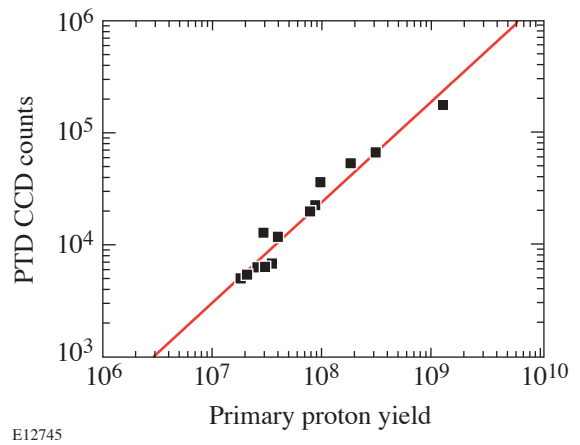


Figure 96.33  
Primary  $\text{D}^3\text{He}$  proton yield measured (CCD counts) by the PTD as a function of yield measured by WRF spectrometers.

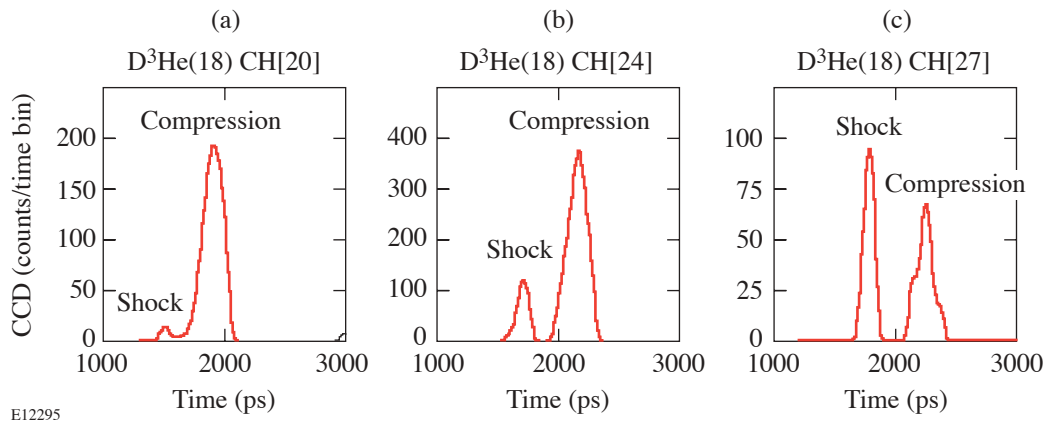


Figure 96.32  
The PTD signal from implosions of plastic shells filled with 18 atm of  $\text{D}^3\text{He}$ : (a) 20- $\mu\text{m}$  shell thickness; (b) 24- $\mu\text{m}$  shell thickness; (c) 27- $\mu\text{m}$  shell thickness.

The time accuracy of the shock and compression burn history in a  $D^3He$  implosion is mainly determined not by the detector itself, but by Doppler and geometrical broadening and  $\rho R$  evolution of the fuel and shell during the implosion.<sup>9,10</sup> The study of  $\rho R$  evolution requires data analysis from many diagnostics and is beyond the scope of this article. A more-detailed study of shock-bang timing and  $\rho R$  evolution is presented in Ref. 10.

### The PTD in $D_2$ Implosions

A typical PTD streak camera image of a  $D_2$  implosion with a neutron yield of  $1.3 \times 10^{11}$  is shown in Fig. 96.34(a) and the deconvolved PTD signal in Fig. 96.34(b). In a  $D_2$  implosion, the first PTD peak is the signal from secondary protons with energies of 12.6 to 17.5 MeV, and the second peak is the signal from the DD neutrons with an energy of 2.45 MeV. Although the yields of secondary protons and primary neutrons differ by

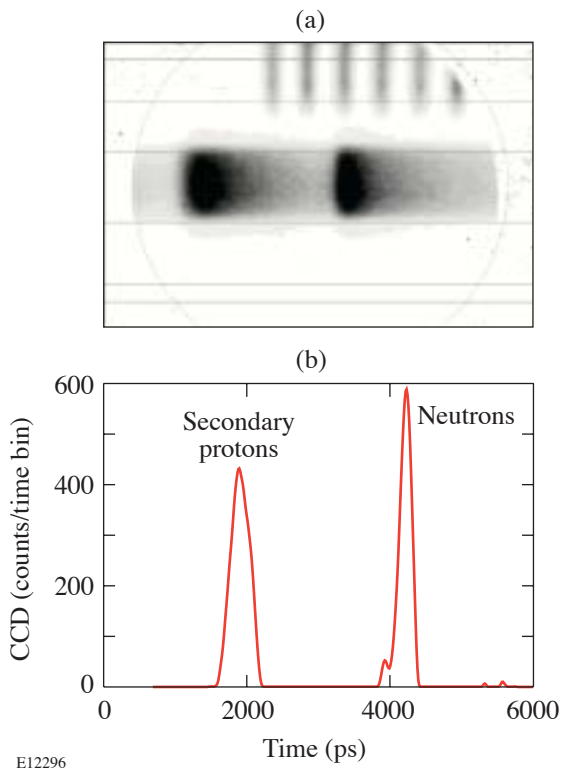


Figure 96.34

(a) The PTD streak camera image from a shot in which a 20- $\mu\text{m}$ -thick plastic shell filled with 15 atm of  $D_2$  was imploded on OMEGA with a 1-ns pulse shape and 23-kJ energy; (b) the PTD signal in this  $D_2$  implosion. From the time-of-flight difference between the secondary-proton and the primary-neutron peaks, the average energy downshift of the secondary protons can be inferred.

a factor of 1000, the PTD signals are comparable due to the different interaction mechanisms of protons and neutrons with the scintillator.

The PTD neutron signal from a  $D_2$  implosion can be used to determine the peak of neutron production (bang time) similar to NTD.<sup>6</sup> Figure 96.35 shows a comparison of the neutron bang time measured by PTD and NTD. The error bars on this plot are 25 ps for NTD and for PTD. The bang times measured by PTD are very close to the bang times from NTD, showing only a 28-ps rms spread. Although temperature broadening of the neutron signal in the PTD is much higher than in the NTD due to different standoff distances (9 versus 2 cm), the PTD bang time is as accurate as the NTD bang time, but the neutron burn width is systematically larger in the PTD than in the NTD due to temperature (or Doppler) broadening.

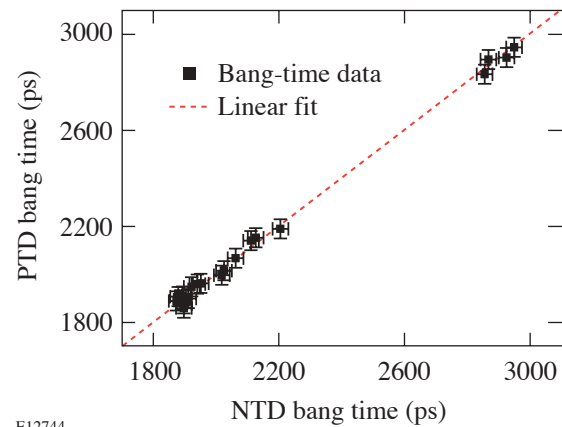


Figure 96.35

Comparison between the neutron bang times measured by the PTD and by the NTD in  $D_2$  implosions on OMEGA.

The secondary proton peak in the PTD signal can be used to measure the secondary-proton yield in  $D_2$  implosions. The number of CCD counts in the PTD for the 1-mm BC-422 scintillator and the filter configuration of 100  $\mu\text{m}$  of Al + 100  $\mu\text{m}$  of Ta is plotted against the secondary proton yield from the WRF spectrometers in Fig. 96.36. The PTD can measure the secondary proton yields in  $D_2$  implosions above  $1 \times 10^7$ .

The average energy downshift of the secondary protons from a  $D_2$  implosion is routinely used on OMEGA to measure the total areal density of the capsule.<sup>16</sup> The average energy downshift of the secondary protons can be inferred from the PTD based on the time-of-flight difference between the sec-

ondary proton and the primary neutron peaks [see Fig. 96.34(b)]. From the secondary proton's energy downshift, the total areal density can be calculated by using plasma-stopping formulas<sup>17</sup> in the same way as done with the WRF data.<sup>16</sup> Figure 96.37 compares the total-areal-density data inferred from the charged-particle spectrometers and the PTD. The comparison is not as favorable as that between the neutron bang times in the NTD and PTD due likely to known areal-density asymmetries<sup>18</sup> on OMEGA.

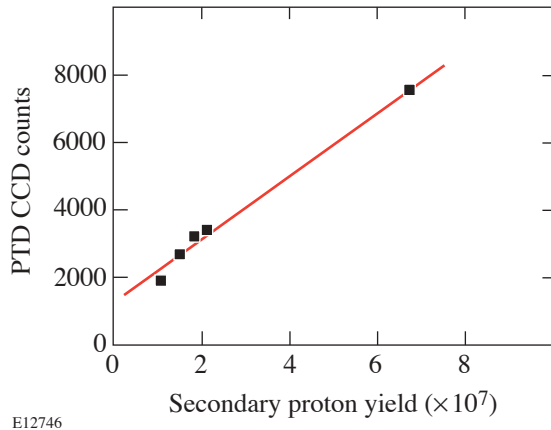


Figure 96.36  
Secondary  $D^3He$  proton yield measured (CCD counts) by the PTD as a function of yield measured by WRF.

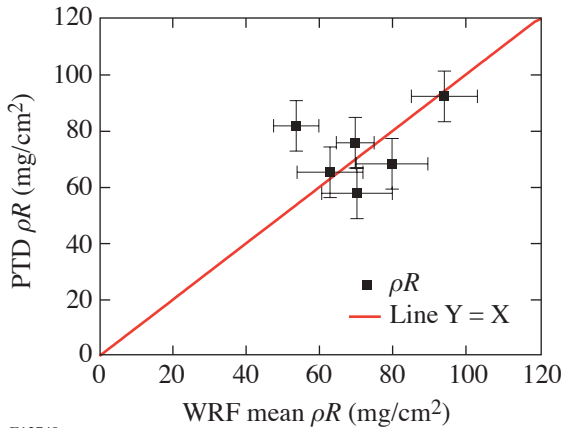


Figure 96.37  
Comparison between average total  $\rho R$  measured by the PTD and by the WRF in  $D_2$  implosions.

## Conclusions and Outlook

A new proton temporal diagnostic (PTD) has been developed to measure the proton burn history in ICF implosions on OMEGA. The PTD nose cone consists of a filter foil sandwich, a scintillator, and the front end of the optical relay system. This hardware is mounted in a TIM and inserted close to the target. The back end of the optical system with an optical streak camera to record the light emitted from the scintillator is mounted outside the vacuum of the target chamber. The OMEGA fiducial system is used to cross-time the x-ray, proton, and neutron signals to the incident laser pulse. An absolute timing accuracy of better than 10 ps has been achieved during the PTD calibration with 100-ps laser pulses. The PTD is able to measure the proton burn history at yields above  $5 \times 10^5$  for  $D^3He$  implosions and resolve shock and compression yields. In  $D_2$ -filled-capsule implosions including cryogenic targets, the PTD can simultaneously measure neutron bang time, neutron yield, secondary-proton yield, and average total areal density.

This article has described the first implementation of the PTD on OMEGA. The PTD standoff distance can be minimized to decrease the thermal broadening and to better fit the requirements of an experiment. Future optimization of the PTD x-ray filter is also possible. In retrospect, the choice of a Ta filter does not appear to be optimal since Al is now needed in front to absorb suprathreshold electrons. A sandwich of aluminum and gold foils will probably be superior. The PTD optimization on OMEGA will be continued in the future.

## ACKNOWLEDGMENT

This work was supported by the U.S. Department of Energy Office of Inertial Confinement Fusion under Cooperative Agreement No. DE-FC03-92SF19460, the University of Rochester, and the New York State Energy Research and Development Authority. The support of DOE does not constitute an endorsement by DOE of the views expressed in this article.

## REFERENCES

1. J. Nuckolls *et al.*, *Nature* **239**, 139 (1972).
2. J. D. Lindl, *Phys. Plasmas* **2**, 3933 (1995).
3. P. W. McKenty, V. N. Goncharov, R. P. J. Town, S. Skupsky, R. Betti, and R. L. McCrory, *Phys. Plasmas* **8**, 2315 (2001).
4. F. H. Séguin, J. A. Frenje, C. K. Li, D. G. Hicks, S. Kurebayashi, J. R. Rygg, B.-E. Schwartz, R. D. Petrasso, S. Roberts, J. M. Soures, D. D. Meyerhofer, T. C. Sangster, J. P. Knauer, C. Sorce, V. Yu. Glebov, C. Stoeckl, T. W. Phillips, R. J. Leeper, K. Fletcher, and S. Padalino, *Rev. Sci. Instrum.* **74**, 975 (2003).

5. T. R. Boehly, D. L. Brown, R. S. Craxton, R. L. Keck, J. P. Knauer, J. H. Kelly, T. J. Kessler, S. A. Kumpan, S. J. Loucks, S. A. Letzring, F. J. Marshall, R. L. McCrory, S. F. B. Morse, W. Seka, J. M. Soures, and C. P. Verdon, *Opt. Commun.* **133**, 495 (1997).
6. R. A. Lerche, D. W. Phillion, and G. L. Tietbohl, *Rev. Sci. Instrum.* **66**, 933 (1995).
7. C. Stoeckl, V. Yu. Glebov, S. Roberts, T. C. Sangster, R. A. Lerche, R. L. Griffith, and C. Sorce, *Rev. Sci. Instrum.* **74**, 1713 (2003).
8. R. D. Petrasso, J. A. Frenje, C. K. Li, F. H. Séguin, J. R. Rygg, B. E. Schwartz, S. Kurebayashi, P. B. Radha, C. Stoeckl, J. M. Soures, J. Delettrez, V. Yu. Glebov, D. D. Meyerhofer, and T. C. Sangster, *Phys. Rev. Lett.* **90**, 095002 (2003).
9. V. A. Smalyuk, P. B. Radha, J. A. Delettrez, V. Yu. Glebov, V. N. Goncharov, D. D. Meyerhofer, S. P. Regan, S. Roberts, T. C. Sangster, J. M. Soures, C. Stoeckl, J. A. Frenje, C. K. Li, R. D. Petrasso, and F. H. Séguin, *Phys. Rev. Lett.* **90**, 135002 (2003).
10. J. A. Frenje, "Measuring Shock-Coalescence Timing and  $\rho R$  Evolution of D<sup>3</sup>He Implosions on OMEGA," to be published in *Physics of Plasmas*.
11. R. A. Lerche and R. L. Griffith, in *High Speed Photography, Videography, and Photonics V*, edited by H. C. Johnson (SPIE, Bellingham, WA, 1987), Vol. 832, pp. 266–274.
12. Goodfellow Corporation, Berwyn, PA 19312-1780.
13. C. Stoeckl, R. E. Bahr, B. Yaakobi, W. Seka, S. P. Regan, R. S. Craxton, J. A. Delettrez, R. W. Short, J. Myatt, A. V. Maximov, and H. Baldis, *Phys. Rev. Lett.* **90**, 235002 (2003).
14. W. R. Donaldson, R. Boni, R. L. Keck, and P. A. Jaanimagi, *Rev. Sci. Instrum.* **73**, 2606 (2002).
15. D. D. Meyerhofer, J. A. Delettrez, R. Epstein, V. Yu. Glebov, V. N. Goncharov, R. L. Keck, R. L. McCrory, P. W. McKenty, F. J. Marshall, P. B. Radha, S. P. Regan, S. Roberts, W. Seka, S. Skupsky, V. A. Smalyuk, C. Sorce, C. Stoeckl, J. M. Soures, R. P. J. Town, B. Yaakobi, J. D. Zuegel, J. Frenje, C. K. Li, R. D. Petrasso, D. G. Hicks, F. H. Séguin, K. Fletcher, S. Padalino, M. R. Freeman, N. Izumi, R. Lerche, T. W. Phillips, and T. C. Sangster, *Phys. Plasmas* **8**, 2251 (2001).
16. F. H. Séguin, C. K. Li, J. A. Frenje, S. Kurebayashi, R. D. Petrasso, F. J. Marshall, D. D. Meyerhofer, J. M. Soures, T. C. Sangster, C. Stoeckl, J. A. Delettrez, P. B. Radha, V. A. Smalyuk, and S. Roberts, *Phys. Plasmas* **9**, 3558 (2002).
17. C. K. Li and R. D. Petrasso, *Phys. Rev. Lett.* **70**, 3059 (1993).
18. F. H. Séguin, C. K. Li, D. G. Hicks, J. A. Frenje, K. M. Green, R. D. Petrasso, J. M. Soures, D. D. Meyerhofer, V. Yu. Glebov, C. Stoeckl, P. B. Radha, S. Roberts, C. Sorce, T. C. Sangster, M. D. Cable, S. Padalino, and K. Fletcher, *Phys. Plasmas* **9**, 2725 (2002).